2025-09-04

Progress Towards Confinement of an Ultracold Neutral Plasma with Electric and Magnetic Fields

Ben Farley
Brigham Young University

Progress Towards Confinement of an Ultracold Neutral Plasma with Electric and Magnetic Fields

Benjamin Farley

A thesis submitted to the faculty of
Brigham Young University
in partial fulfillment of the requirements for the degree of

Master of Science

Scott Bergeson, Chair
Justin Peatross
Michael Ware

Department of Physics and Astronomy

Brigham Young University

ABSTRACT

Progress Towards Confinement of an Ultracold Neutral Plasma with Electric and Magnetic Fields

Benjamin Farley
Department of Physics and Astronomy, BYU
Master of Science

Ultracold neutral plasmas represent a regime of plasmas that is not entirely described by theory, but is critical to our understanding of many phenomena. Though their low temperature makes observing them more manageable, even "confined" ultracold plasmas do not remain contained for more than a few hundred microseconds. No steady state or long-term confinement of an ultracold plasma created by pulse ionization has ever been demonstrated. In this thesis, the construction of a Penning trap for calcium ultracold neutral plasma is presented. The trap consists of a uniform magnetic field to trap the electrons radially and a quadrupole electric field to trap them in the axial direction, under the hypothesis that the space charge of the electrons will trap the ions. To the best of the author's knowledge, no ion trap of this configuration has been used to confine ultracold neutral plasmas. In addition to the Penning trap, this thesis also presents work done on other projects. This includes data acquisition and analysis on freely expanding ultracold neutral plasmas with varying density gradients, research on dielectric discharge barrier plasmas, and presentations given on these subjects. Finally, a short list of skills developed over the course of this program is given.

Keywords: ultracold neutral plasma, magnetized plasma, Penning trap, plasma confinement, strong coupling

ACKNOWLEDGMENTS

I would not have been able to complete this program without the help of many talented and gracious individuals. Dr. Bergeson, my advisor, is the most competent scientist I have ever had the pleasure of working with, and yet somehow he manages to be an even better mentor and human being. I am grateful for the time he took to teach me and for his example and enthusiasm for science. Additionally, I want to thank my committee, comprised of Dr. Bergeson, Dr. Peatross, and Dr. Ware, for giving me the encouragement I needed to finish this program.

I also want to thank my family, especially my parents, David and Ann Farley, for their unwavering support and for the many last-minute babysitting requests that they accepted. And to my children: you are the entire reason I keep going.

Finally, I want to thank my Heavenly Father and recognize His hand in my life.

This work was supported in part by the BYU Department of Physics and also by the National Science Foundation under Grant No. NSF-2009999.

Contents

List of Figures

Chapter 1

Ultracold Neutral Plasma Confinement with a Penning Trap

1.1 Introduction

The main thrust of my research has been in the construction of a new experiment, wherein electric and magnetic fields are used to trap an ultracold neutral plasma (UNP) of calcium. UNPs remain an active area of research, in part due to their accessibility as benchmarks for testing predictions, validating models, and studying strongly-coupled systems in a controlled environment [1]. However, UNPs have proven difficult to confine. This experiment was designed to increase the trap lifetime of UNPs using a setup similar to a Penning trap, though one that is specifically calibrated to trap electrons instead of positively charged ions. Utilizing the space charge of the trapped electrons to keep the ions from escaping the plasma may be more akin to an electron beam ion trap (EBIT) than a Penning trap, so this chamber will be referred to as an "electron Penning trap" throughout this work. The author is unaware of any such design for trapping UNPs in the literature.

Generally speaking, a Penning trap combines a uniform magnetic field with a static electric field to confine charged particles [2]. While UNPs do not have an overall charge (at least, not immediately after ionization), the separation of electrons and ions within the plasma allows ambipolar electric fields to affect the system [3]. In UNPs that are allowed to expand freely, electrostatic pressure, ambipolar fields, and thermal effects within the plasma accelerate the electrons much faster than the ions, by virtue of the ion-electron mass ratio in calcium being approximately $\frac{m_{\mathrm{Ca}}}{m_e} \approx 7.29 \times 10^4$. As electrons are accelerated out of the plasma, the system becomes non-neutral, leading to weaker electron screening and greater ion-ion repulsion [4]. Essentially, the ions "follow" the electrons out of the system. For this reason, the electron Penning trap used in this experiment was designed to hinder electrons from leaving the plasma.

For this experiment, a Helmholtz configuration was used to create a uniform magnetic field to confine the electrons radially. Two electrodes (thin metallic screens) kept at a negative voltage provided the quadrupole electric field to confine the electrons in the axial direction, as shown in Fig. 1.1. Additionally, two magnetic coils in an anti-Helmholtz configuration were used to trap the neutral calcium atoms in a magneto-optical trap (MOT) prior to ionization, as explained in Section 1.3.

1.2 Constructing the Chamber

UNPs are created in high vacuum environments. The vacuum chamber used for this experiment is made of stainless steel and consists of 14 main ports. On one port, a hollowed-out flange containing the calcium sample was attached behind a gate valve, separating the calcium from the rest of the chamber. This allows for the sample's removal without the need to bring the entire chamber back up to atmospheric pressure. A right-angle bellows valve and an ion pump are also attached here. The right-angle valve allows for the connection of a roughing pump to get the pressure low enough for

the ion pump to be safely engaged. Similarly, another right-angle valve and ion pump were attached to another port to evacuate the rest of the chamber.

In front of the calcium sample, an additional flange with a triangular nozzle was installed. This nozzle contains 120 small tubes to help collimate the atomic beam into the center of the chamber. A flange heater was installed around the connection of these two flanges to heat the calcium sample to 570°C in order to provide a consistent atomic beam and to prevent calcium buildup in the nozzle. The port opposite the atomic beam was fitted with another flange heater at 100°C to prevent calcium deposition on the window.

Before the chamber could be evacuated, the electrodes and the magnetic coils used to generate the uniform magnetic field had to be installed, as seen in Fig. 1.1. The vacuum chamber is held at ground potential. The screens that served as the electrodes were mounted onto an insulating material with epoxy. A 14 AWG copper wire was also attached via epoxy and connected to an electrical throughput. This setup proved to be quite fragile and required the chamber to be opened a number of times in order to be repaired. These seeming setbacks provided an opportunity to reassess the setup, and, at Dr. Peatross' suggestion, led to a new design of smaller electrodes. This was done to avoid the "two infinite plane" approximation, wherein the electric field between two infinite planes held at the same potential is $0\,\mathrm{V/m}$ everywhere.

1.3 The Magneto-optical Trap (MOT)

To create a UNP, there first has to be neutral atoms trapped in the center of the chamber. This is done using a magneto-optical trap (MOT), which exploits the Doppler effect and the Zeeman effect in tandem to cool and trap atoms [5]. A 423 nm slower laser, detuned from atomic resonance by about 300 MHz using an acousto-optic modulator is blue-shifted into resonance with the incoming atoms, which enter the chamber with an average velocity of over $400\,\mathrm{m/s}$. As the atoms absorb the

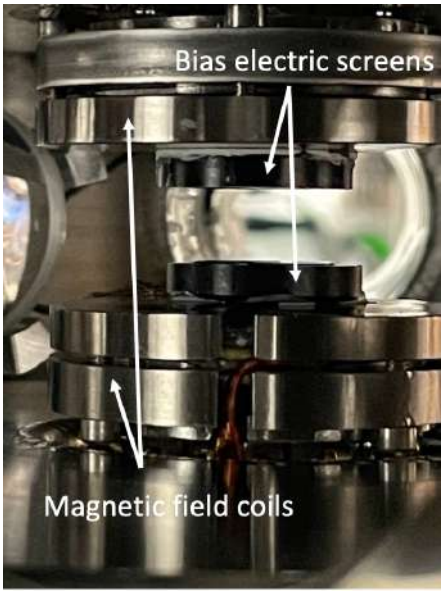

Figure 1.1 Photo of the inside of the vacuum chamber. The screens that provide the bias electric field are embedded in the two black rings nearest the center of the chamber. The screens are insulated from the rest of the chamber. The Helmholtz coils that provide the magnetic field are inside the cylinders that the rings are attached to.

photons from the slower laser and then reemit those photons isotropically, the net result is a loss of momentum in the reference frame of the laboratory. As the calcium atoms slow down, they would quickly fall out of resonance with the slower laser were it not for a graded magnetic field generated by the two anti-Helmholtz coils on the outside of the chamber. This spatially-varying magnetic field introduces a Zeeman shift in the energy levels of the calcium atoms, which compensates for the decrease in the Doppler shift. The atoms will remain in resonance with the slower laser if the interplay between the Zeeman shift and Doppler shift can satisfy the Zeeman scattering condition,

$$\omega_L = \omega_0 + \Delta\omega_D + \Delta\omega_Z \tag{1.1}$$

where ω_L is the frequency of the slower laser, ω_0 is the field-free atomic resonance, $\Delta\omega_D$ is the Doppler shift, and the Zeeman shift is $\Delta\omega_Z = \frac{\mu_0 m_j g_L B(x)}{\hbar}$. As long as the strength of the magnetic field is enough to induce an energy shift that equals the Doppler shift of the neutral atoms, they

will continue to interact with the slower laser as they travel towards the center of the chamber. The atoms' velocity is greatly reduced by the time they reach the trapping location of the MOT.

In the center of the chamber, six orthogonal 423 nm lasers intersect, as shown in Fig. 1.2. Instead of being detuned by 300 MHz like the slower laser, these trapping lasers are detuned by about 64 MHz. This means that a calcium atom traveling at around 27 m/s toward one of these lasers would be exactly on resonance with it, according to the non-relativistic Doppler shift,

$$v = \frac{\Delta\nu}{\nu_0} \cdot c \tag{1.2}$$

where $\nu_0 = \frac{c}{\lambda}$ and $\Delta\nu = 64\,\text{MHz}$. However, due to the 35 MHz natural line width of neutral calcium, atoms moving much slower than this still have an appreciable chance of interacting with the laser photons and slowing down. This velocity-dependent damping force is called "optical molasses" [6].

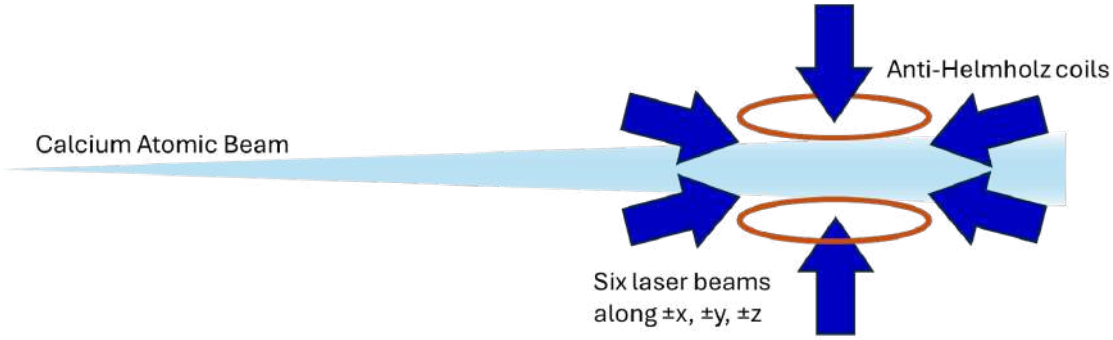

Figure 1.2 Six orthogonal 423 nm lasers trap and cool the neutral calcium atoms. The Doppler effect provides velocity-dependent damping of the atoms.

The other component of trapping neutral atoms in a MOT is the spatially-dependent restoring force provided by the trapping lasers. In the center of the chamber, the quadrupole magnetic field is 0 and increases linearly in magnitude over the size of the trap. This size is generally on the order of 1 mm in diameter. As the calcium atoms wander towards the edge of the trap, the increasing magnetic field causes a Zeeman shift that puts the atoms in resonance with the laser. A magnetic field of about 2.86 mT is sufficient to put the atoms in resonance.

State selective radiation allows the Zeeman-shifted atoms to interact with the appropriate laser and be pushed back into the trap, rather than out of it. The 423 nm transition is not simply Zeeman shifted, but Zeeman *split* according to the magnetic quantum number m_j. Right-circularly polarized light, σ_+ carries $\hbar$ angular momentum, and so, by selection rules, can interact with $m_j = -1$ or $m_j = 0$ atoms but not $m_j = 1$ atoms for a transition from a j=0 to j=1 state,. The opposite is true for σ_- light, which carries a momentum of $-\hbar$. Figure 1.3 shows how the Zeeman splitting, combined with the polarization of the light, allows us to control which laser the atoms will interact with. This ensures a restoring force towards the center of the trap rather than a force to expel the atoms out of it.

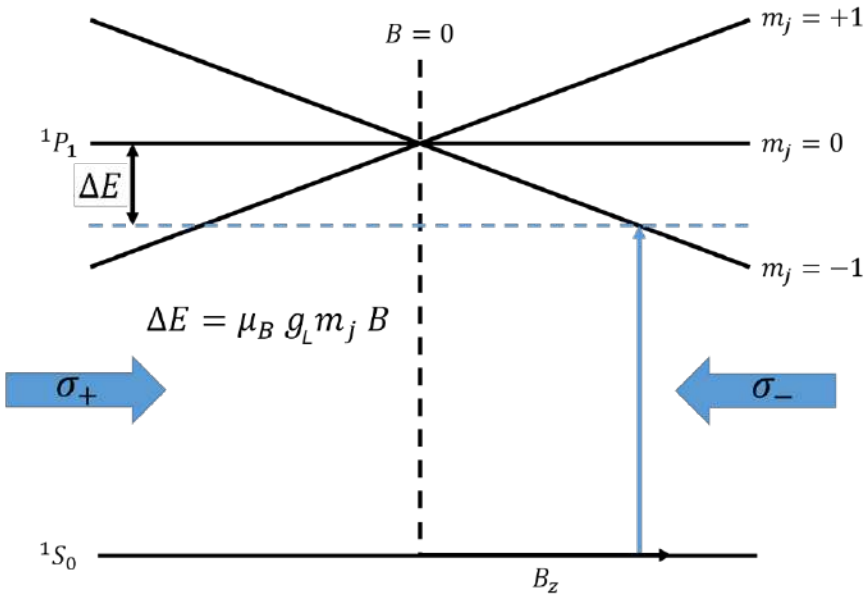

Figure 1.3 The combination of Zeeman splitting and circularly polarized light allows for spatially selective interaction with the 423 nm laser light. Atoms at the edge of the trap will be pushed back toward the center. The shift in energy is given by the equation for ΔE, where μ_B is the Bohr magneton, g_L is the Landé g factor, m_j is the magnetic quantum number, and B is the magnetic field strength. This figure is from [7].

The circular polarization of the trapping lasers is achieved through the use of quarter-wave plates (QWP). A QWP alters the polarization state of light by introducing a 90° phase shift between

its orthogonal polarization components, relative to the plate's fast and slow axes. This phase shift causes the resultant electric field vector to rotate. From the point of view of the atoms looking toward the laser beam source, an incoming beam whose electric field vector is rotating counter clockwise is σ_+ light, while an electric field vector that is rotating clockwise is σ_- light. Counter propagating beams must have opposite polarization for the MOT to work. Instead of using six trapping lasers (which would require careful calibration of six QWPs), flat mirrors were used to retroreflect the three orthogonal lasers (labeled East/ West, North/South, and top/bottom) back through the chamber. This reduced the number of optics equipment on the table as well as the number of adjustable parameters needed to make the MOT function. Although this configuration still requires six QWPs, only three of them needed to be set at the correct angle. Appendix A contains a proof that light passing through a QWP set at any arbitrary angle and then retroreflecting back through it will result in an opposite polarization of that light (i.e., the "handedness" of the light is reversed).

To get a stable MOT using a retroreflective mirror system, it is important that the reflection be anti-parallel with the incoming beam. This proved challenging at first, as the reflections were difficult to differentiate from the incoming beams. However, it was discovered that precise alignment of the beams could be achieved by sending the laser through a small aperture. This caused the incoming beam and the reflected beam to become visible as distinct points, which could then be overlapped at a considerable distance from the chamber. Proper alignment, polarization, and power balance of the trapping lasers are all required for the MOT to function. An optimized MOT is shown in Fig. 1.4.

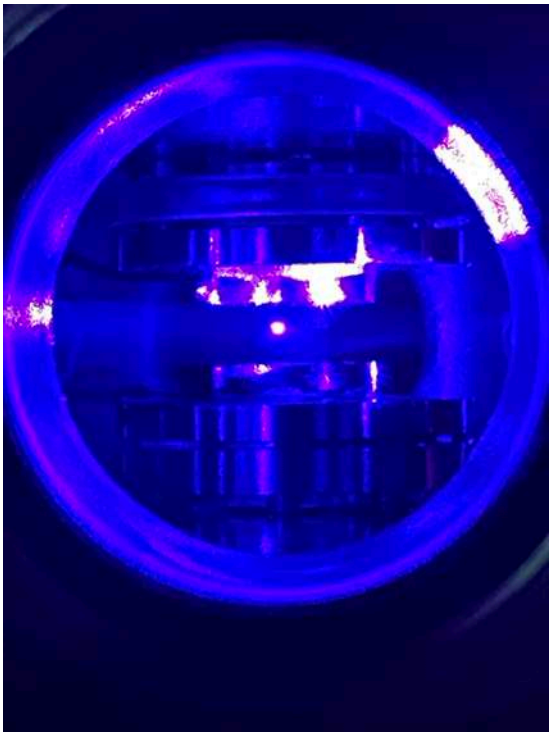

Figure 1.4 Photo of 423 nm fluorescence from neutral calcium atoms in the MOT.

1.4 Electrical Circuits

Because this experiment requires fast switching for magnetic coils (the MOT coils for the neutral atoms and the bias coils for the ions), two custom electrical circuits had to be built in the laboratory. These circuits had to be able to withstand a load of nearly 200 A, meaning their resistive components had to be water cooled. This was done by mounting the components on custom-built aluminum blocks, connecting the blocks to the laboratory's chilled water system with polyurethane tubing, and expending copious amounts of paper towels on a seemingly unending series of leaks and water line failures. The circuits also had to be able to ramp up solenoids in under 500 μs, so fast IGBT switches were used. A blueprint for building these circuits had been created by Tucker Sprenkle some years earlier in his Ph.D. dissertation [7].

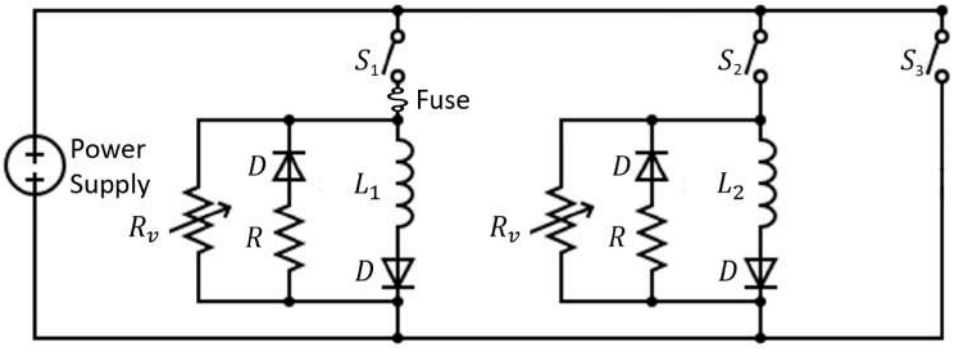

Figure 1.5 Diagram of the electrical circuit used for the bias magnetic coils inside the chamber. Diodes (able to withstand current of 300 A) are labeled D, resistors (1Ω) are labeled R, R_v is for varistor, and S is the IGBT switch. The magnetic field coils are labeled as L1 and the inductive resistor used as an intermediate current ramping stage is L2. This figure is reproduced from [7].

A pulse generator is used to turn off the MOT coils just before the neutral calcium atoms are ionized. This way, the B-field from the MOT does not interfere with the B-field of the bias coils during confinement. In order to ensure proper ramp up time for the bias coils, a short circuit was built in series with an intermittent ramp up stage, which is essentially identical to the circuit for the bias coils (see Fig. 1.5). This ramp up stage allows for the power supply to reach the correct output voltage before putting current through the bias coils. A power supply must charge or discharge its capacitors to respond to changes in load conditions, such as resistance or back EMF from inductive loads [7]. This process follows an exponential time dependence governed by the equation,

$$I(t) = I_{\text{final}}\left(1 - e^{-t/\tau}\right), \quad \text{where } \tau = \frac{L}{R} \tag{1.3}$$

the bias coils inside the chamber have an inductance $L = 100\,\mu\text{H}$ and resistance $R = 0.09\,\Omega$. Therefore, we get a ramp up time of 0.9 ms.

Initially, switch 3 is the only switch that is closed, forming the short circuit. When the pulse generator signals for switch 2 to close, switch 3 is signaled to open $15\,\mu$s later, causing the current

to flow into the ramp up stage circuit. The inductance of the water-cooled "dummy coil" L_2 requires the power supply to adjust its voltage to output the set amperage. This process is given 20 ms to occur, which is more than ample time for the power supply to respond. At this point, switch 1 is closed and 15 μs later, switch 2 is opened. If the resistance and inductance of L_1 and L_2 are equal (or nearly so), then the power supply should not have to make any more adjustments to ramp up the bias coils. We measured our ramp up time to be about 400 μs, comfortably under the 500 μs requirement. Figure 1.6 shows this timing schematic.

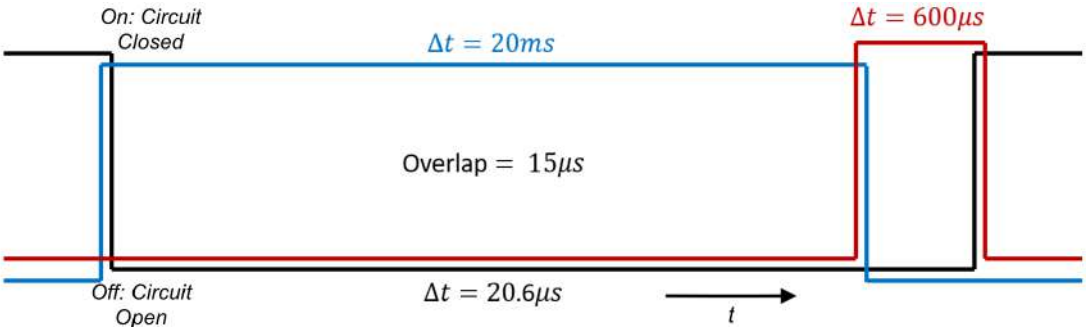

Figure 1.6 Diagram of the timing used for the bias coils. The black line represents the short circuit, which remains on until the L_2 inductor circuit is ramped up, represented by the blue line. The red line represents the circuit for the magnetic field coils. Once the current is directed into the magnetic field coils, the plasma is ionized and measurements are taken prior to the circuit opening once again. A 15 μs overlap allows the switches to respond to the signal from the pulse generator. This figure is from [7].

1.5 Modeling- SimIon®

To model the quadrupole electric field inside the chamber, a simulation software called SimIon® was used. This software allows a user to create a virtual environment of charged particles/ objects and map the resulting voltages. It also shows how a charged particle will respond in this environment. It does not, however, provide an accurate visualization of the electric field. To achieve this, a custom script was written in Lua to calculate and plot the electric field using the equation,

$$\vec{E} = -\nabla V \tag{1.4}$$

Further adjustments were required using Lua to ensure proper spacing of the electric field lines and to create a compatible user interface. Once this was accomplished, a to-scale representation of the screens held at bias voltage was created in the program and the electric field was mapped out.

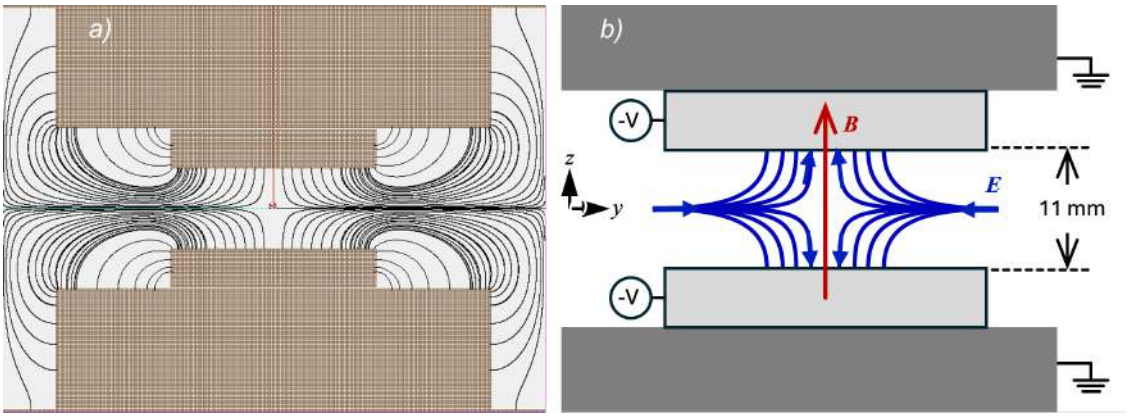

Figure 1.7 a) Simulation of the electric field between the two electrodes using SimIon® software. The black contour lines represent the electric field, with a higher density of field lines representing a stronger field. The thin red and green lines show $x = 0$ and $y = 0$, respectively. **b)** In the electron Penning trap, a uniform magnetic field confines electrons radially, while a bias electric field confines them in the axial direction.

The quadrupole electric field within the chamber should be such that it cancels with the ambipolar field of the plasma. Figure 1.8 shows a comparison of the modeled electric field when the electrodes are held at $-0.2\,\mathrm{V}$ as well as the ambipolar field of the expanding plasma from the hydrodynamic model with $T_e = 100\,\mathrm{K}$. Plasmas in our lab rarely exceed an electron temperature of $100\,\mathrm{K}$, hence, relatively weak electric fields are sufficient to cancel the ambipolar field that drives ion expansion.

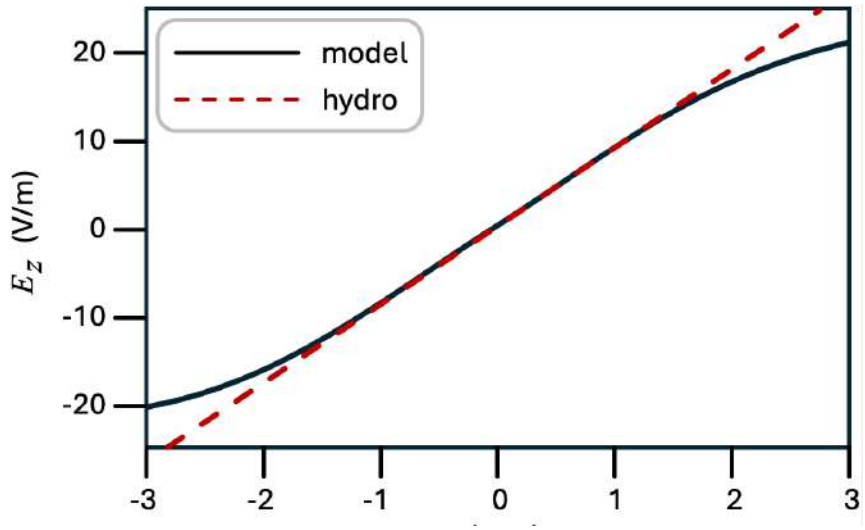

Figure 1.8 Electric field vs. position, measured from the center of the chamber. The solid black line shows the quadrupole field from the electrodes when held at $-0.2V$. The dashed red line shows the ambipolar field from the plasma.

1.6 Optics Setup

In addition to the slower laser and trapping lasers mentioned in Section 1.3, four other lasers are needed for the electron Penning trap to function. Two pulsed dye lasers are used for photo-ionization, an 866 nm repumper laser is used to keep the singly-ionized Ca^+ ions from accumulating in a metastable "dark state", and a 397 nm probe laser excites the Ca^+ ions and causes them to fluoresce. This gives us our signal that we will use to determine the lifetime of the plasma.

1.6.1 Ionizing Lasers

For ionization, a 423 nm laser pulse excites atoms into the $4s4p\,^1P_1$ state, while a 390 nm pulse takes the electrons from this state and excites them just above the ionization threshold, as seen in Fig. 1.9. The electron temperature of the plasma can be adjusted by tuning the frequency of the 390 nm laser.

The shape and timing of the 423 nm and 390 nm pulses greatly affects the ionization of the calcium sample in the MOT. Because these pulses originate from two different dye lasers, they

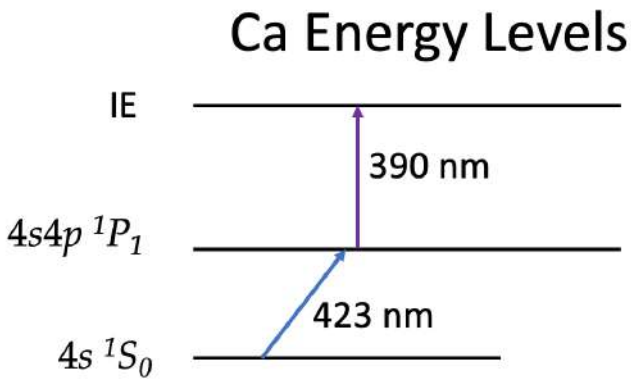

Figure 1.9 Partial energy level diagram for the ionization of neutral calcium. Electron temperature is determined by how far the electrons are excited above the ionization energy (IE) theshold.

are superimposed using a dichroic filter. This filter reflects impinging 390 nm light and transmits 423 nm light. The path length of the lasers must be calibrated for the two pulses to arrive at the sample at the same time. Because the pulses naturally diverge, a telescoping lens system was put in place to collimate the light.

1.6.2 Using Optical Telescopes

The simplest version of a telescoping lens system creates 1:1 imaging by using two identical convex lenses set at a distance $2f$ apart, where f is the focal length of the lenses (see Fig. 1.10). The first lens in the telescope is placed a distance f from the object so as to create an identical (inverted) image a distance f after the second lens. In the context of lasers, collimated light coming into an ideal telescope will also emerge collimated, but by adjusting the distance between the lenses, one can control the convergence/ divergence of the outgoing beam. Moreover, by using lenses of differing focal lengths and separating them by a distance of $f_1 + f_2$, one can magnify the size of the

beam by a factor of $\frac{f_2}{f_1}$. A telescope was used give the slower laser a slight convergence as it passed through the chamber, as this increased its efficacy in interacting with the atomic beam.

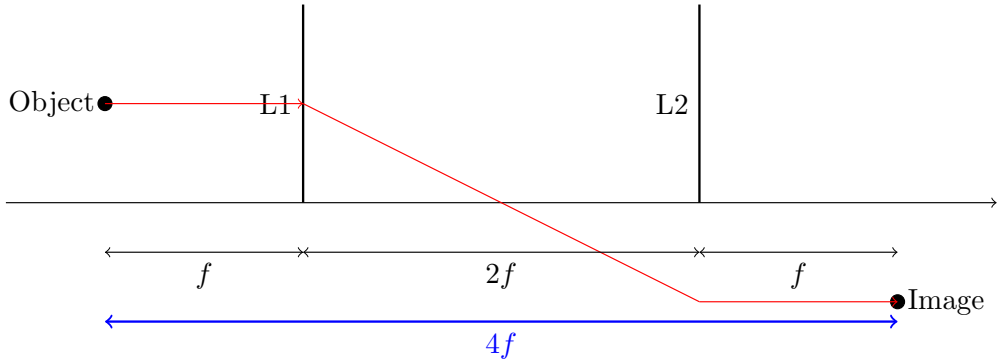

Figure 1.10 Ray trace diagram of an ideal telescoping lens system. The convergence/ divergence of an incoming laser beam can be controlled by adjusting the distance between the two lenses L_1 and L_2. The expansion/ compression of the beam can be controlled by using lenses of differing focal length f, with a separation distance of $f_1 + f_2$ between the beams.

1.6.3 Probe Laser & PMT

Once the calcium has been ionized, a 397 nm probe laser is used to excite the ions, which creates a fluorescence signal as the ions decay back down to the ground state. A telescoping lens system inside the chamber focuses the fluorescence onto a PMT outside the chamber, with excess scattered light being blocked by an adjustable aperture. This signal is the primary source of data for this experiment; as long as there are calcium ions in the trap that are being illuminated by the probe laser, the PMT will register a fluorescence signal. A similar telescope on the other side of the chamber can be utilized to provide data to an ICCD camera, should the need arise in future experiments. PMTs are detectors with extremely high temporal resolution, making them ideal for capturing fast intensity changes but without spatial information. ICCD cameras, in contrast, provide two-dimensional spatial mapping of light intensity, with the ability to gate exposures for time-resolved imaging. Used

together, they can provide corroborating data of plasma phenomena. For this experiment, however, only the PMT was used for data acquisition.

In addition to acquiring fluorescence data, the PMT can also be used to measure the percentage of calcium ionization occurring in the trap. A 423 nm bandpass filter was placed in front of the PMT to allow only fluorescence from the neutral atoms in the MOT to pass through. By marking the fluorescence signal on the oscilloscope, and then noting the change in the signal after the ionizing pulses are allowed to enter the chamber, the overall ratio of atoms to ions can be obtained. A decrease in MOT fluorescence indicates that the atoms have been ionized and no longer fluoresce at 423 nm, though the current configuration only allows one wavelength of fluorescence to be detected at a time. To increase the ionization percentage, a retroreflective mirror was placed to reflect the pulses back onto the MOT. Once a sufficient level of ionization is achieved, the 423 nm bandpass filter on the PMT is exchanged for a 397 nm bandpass filter to observe ion fluorescence directly.

1.6.4 866 nm Ion Repumper

Both neutral Ca and singly-ionized Ca^+ have loss channels that can undermine UNP experiments. In neutral calcium, the $4s4p\,^1P_1$ atoms excited by the 423 nm laser can decay into the $3d4s\,^1D_2$ metastable state, which is known as a "dark state" because it essentially removes atoms from the cooling cycle. For ionized calcium, the $4\,^2P_{1/2}$ excited state has about a 6% chance of decaying into the $3\,^2D_{3/2}$ excited state, another dark state that removes those ions from the system (see Fig. 1.11). This transition emits photons with a wavelength of 866 nm. A repumper laser at this same wavelength puts the ions that decay through this loss channel back into $4\,^2P_{1/2}$ state, where they will likely decay down into the ground state again. Due to resource constraints in the lab, the neutral calcium loss channel is not repumped.

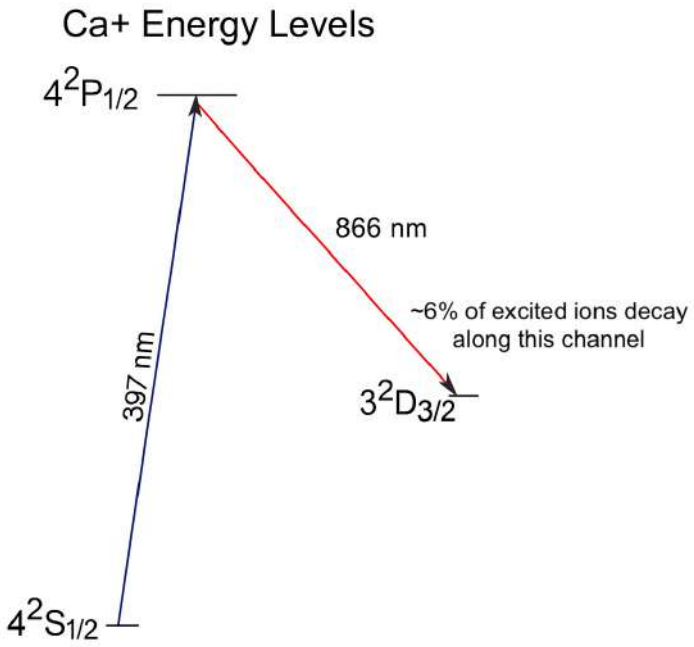

Figure 1.11 Partial energy level diagram of singly-ionized calcium. The 866 nm repumper laser "plugs" the loss channel from the $4\,^2P_{1/2}$ state to the $3\,^2D_{3/2}$ state.

1.7 Next Steps

In order to start collecting data, the ionization percentage of the calcium sample must be improved. The highest ionization percentage achieved as of this thesis was around 40%. Ideally, total ionization should be reached before beginning the experiment. As described previously, the easiest way to determine the fraction of neutral calcium atoms that are being ionized is by looking at the 423 nm fluorescence on the oscilloscope before and after the ionizing pulses are allowed to enter the chamber. There are several reasons why the ionization percentage may be low, including:

- Poor temporal overlap of the ionizing pulses
- Poor shape/ size of ionizing pulses
- Low power in ionizing pulses

- Improper alignment of periscoping and/ or retroreflective mirror for the ionizing pulses
- Sub-optimal position of MOT

Attempts have been made to redress all of the items above, but with such a sensitive experiment, it is common that the improvement of one aspect of the setup leads to the detriment of another. It is also possible that some other unknown factor not in the list above has impeded an adequate ionization percentage. However, once it has been determined that total (or nearly total) ionization has been achieved, the 423 nm bandpass filter should be swapped for the 397 nm filter. Then recording data on the lifetime of the plasma should be viable.

As many of the laboratory resources are shared between different vacuum chambers, it is important to verify that all the necessary components are connected to the electron Penning trap chamber. This includes: verifying that the proper channels on the pulse generators are selected, verifying that the correct BNC cables are connected to the pulse generators and oscilloscope, optimizing the power coupling of the 423 nm into the chamber, and optimizing the alignment of the pulse lasers after attaching the appropriate mirrors onto their magnetic mounts.

Future experiments may rely on a wider set of available data, such as the volume/ peak density of the MOT, the spatial profile of the plasma, the time evolution of the ion velocity distribution in phase space, etc. Much of the equipment needed to gather these sorts of data is already in place, but needs to be optimized. The mounted ICCD camera would allow for high-resolution, spatially-resolved images of the plasma. A second Blackfly USB camera only needs minor adjustments to obtain 1:1 imaging of the MOT from an angle orthogonal to the first USB camera that is already in place. These two orthogonal images (along with a 423 nm probe laser) would allow for additional information about the MOT to be deduced, such as the overall size, density, and approximate number of atoms in the trap. Should resources become available in the laboratory, a 424 nm repumper laser for the neutral atoms would also be beneficial in increasing the number of atoms in the MOT.

One future experiment that may be of particular interest would be observing the time evolution of phase-space plots of the ion velocity distribution. Such data have been taken for various configurations of freely expanding plasmas in our lab previously and used to validate code used for plasma modeling (described in greater detail in Chapter 2). Such an experiment in the electron Penning trap could lead to a greater understanding of confined UNP behavior and energy transport [4].

1.8 Previous Work on Magnetically Confined UNPs

Our lab and others have done previous work on magnetically confined UNPs, though with different magnetic field configurations than the electron Penning trap. These experiments have shown that the dynamics of magnetized, strongly-coupled plasmas are not fully describable with traditional plasma theory [4]. In a strongly magnetized UNP, for instance, Sprenkle et al. found that the transverse expansion of the plasma slows down dramatically with increasing magnetic field strength, even though the profile of the plasma in both the transverse and longitudinal directions remained Gaussian. It was also found that neither standard diffusion models nor self-similar expansion models accurately described the expansion of the plasma.

In partially magnetized plasmas, other phenomena were observed such as increased electron-ion collision rates due to the magnetic field and transverse breathing modes not coupled to the longitudinal velocity [8]. Figure 1.12 shows the appearance of these transverse modes in the hydrodynamic velocity of the ions in the presence of an intermediate uniform magnetic field.

In addition to the unpredicted phenomena discovered in magnetized UNPs, it was also found that the presence of the cusp field increased the lifetime of the plasma to around $500\,\mu$s, as opposed to a few tens of μs for an unmagnetized UNP [9]. Once in the magnetized cusp trap, however, the strength of the magnetic field did not have a significant effect on the lifetime of the plasma [10].

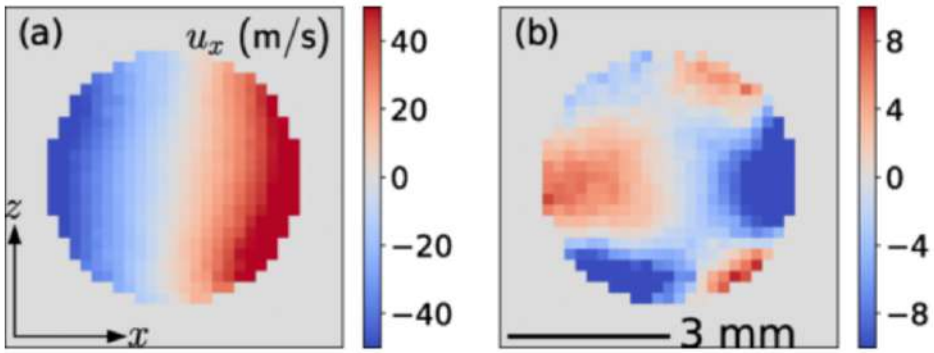

Figure 1.12 False-color images of the hydrodynamic velocity of the ions in a partially magnetized UNP $2\,\mu s$ after ionization. **a)** $B = 0$. The hydrodynamic velocity closely matches the Vlasov model for Gaussian distribution functions. **b)** $B = 183\,\mathrm{G}$. Transverse modes appear in the hydrodynamic velocity. The magnetic field points in the z-direction. This figure was taken from [8].

Chapter 2

BGK Project

2.1 Overview

All plasma models begin with a kinetic equation that can only be solved with approximations. These approximations arise from assumptions that have to be made to make calculations more tractable, but they limit the scope of the model. In order to remedy this, our lab generates high-quality data by creating UNPs and diagnosing them with precision laser spectroscopy. We then provide this data to our collaborators, against which they can validate computational codes. In particular, during my time performing research under Dr. Bergeson, our lab has worked with Dr. Michael Murillo of Michigan State University and Dr. Jeff Haack at the Los Alamos National Laboratory to test and improve kinetic codes in order to more accurately model physical systems. These kinetic codes, known as Bhatnagar-Gross-Krook (BGK) codes, model plasmas by solving the Boltzmann equation to predict their evolution in phase space. The Boltzmann equation (which was originally developed to study the behavior of rarefied gases) is,

$$\frac{\partial f}{\partial t} + \mathbf{v} \cdot \nabla_{\mathbf{r}} f + \frac{\mathbf{F}}{m} \cdot \nabla_{\mathbf{v}} f = \left(\frac{\partial f}{\partial t} \right)_{\text{coll}} \tag{2.1}$$

where $f(\mathbf{r},\mathbf{v},t)$ is the single-particle distribution function in phase space, $\nabla_{\mathbf{r}}$ is the gradient with respect to space, $\nabla_{\mathbf{v}}$ is the gradient with respect to velocity, and $\left(\frac{\partial f}{\partial t}\right)_{\text{coll}}$ is the rate of change of f due to particle collisions (known as the collision term). Various models of fluid mechanics, magnetohydrodynamics, and kinetic plasmas utilize different, solvable approximations of the collision term. The BGK model approximates the Boltzmann collision term as,

$$\left(\frac{\partial f}{\partial t}\right)_{\text{coll}} = -\frac{f - f^{(0)}}{\tau}, \tag{2.2}$$

where $f^{(0)}(\mathbf{r},\mathbf{v},t)$ is the local Maxwell–Boltzmann equilibrium distribution with the same density, mean velocity, and temperature as f, and τ is the relaxation time (mean time between collisions). This form models collisions as a simple relaxation process, driving f toward $f^{(0)}$ over the characteristic time τ, while conserving mass, momentum, and energy. This technique is useful for modeling systems that are initially in a highly non-Gaussian configuration, such as sculpted plasmas with steep density gradients. In our lab, simple gradients are created by imaging a wire onto the plasma. Consequently, the calcium atoms in the gap are not ionized.

If the collision term is set equal to 0 (known as the Vlasov approximation), then the plasma expansion is driven purely by the electron pressure gradient and the ambipolar electric field. This is known as a "ballistic" plasma, and there is no disorder induced heating of the ions. In Fig.2.1, the sharp density gradients in the plasma cause the ions to accelerate ballistically into the gap. If we model this using the Vlasov approximation and assume the average magnetic field to be $\mathbf{B} = 0$, we can use $\mathbf{F} = q\mathbf{E}$ and solve the one-dimensional Boltzmann equation,

$$E_z = -\frac{m}{q}\left(\frac{\frac{\partial f}{\partial t} + v_z\frac{\partial f}{\partial z}}{\left|\frac{\partial f}{\partial v_z}\right|}\right). \tag{2.3}$$

The derivatives of the distribution function $f(z,v_z,t)$ can all be calculated using data taken during the experiment. This allows us to plot the relative electric field inside the gap. As the plasma

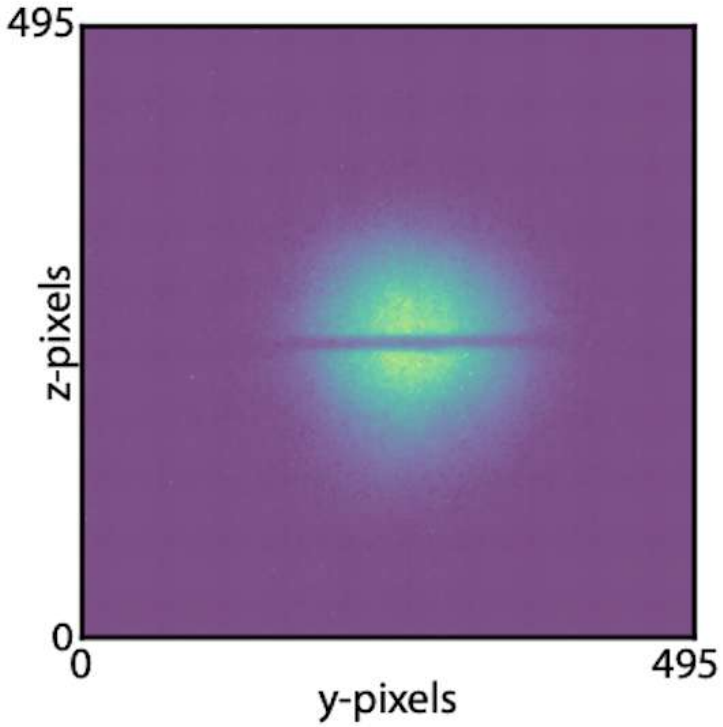

Figure 2.1 P-color plot of the sculpted plasma (also known as the wire plasma) in the yz-plane.

expands and begins to thermalize, however, the ions inside the gap become less ballistic, the Vlasov approximation breaks down, and the electric field results become more suspect.

While the main focus of this project has been to validate and improve BGK codes, it is clear that much can be learned about UNPs from the data itself. Over the past two years, I have aided in acquiring and processing data for this project, as well as consulting in the direction and development of its progression. During this time, our lab has provided data on a rich variety of plasma configurations with differing density gradients. By allowing these plasmas to expand freely and then analyzing the evolution of the ion velocity distribution, we can gain insight into different aspects of UNPs, such as electron-ion thermalization properties, the relative electric field strength within the plasma, stopping power across sharp density gradients, and energy transport properties.

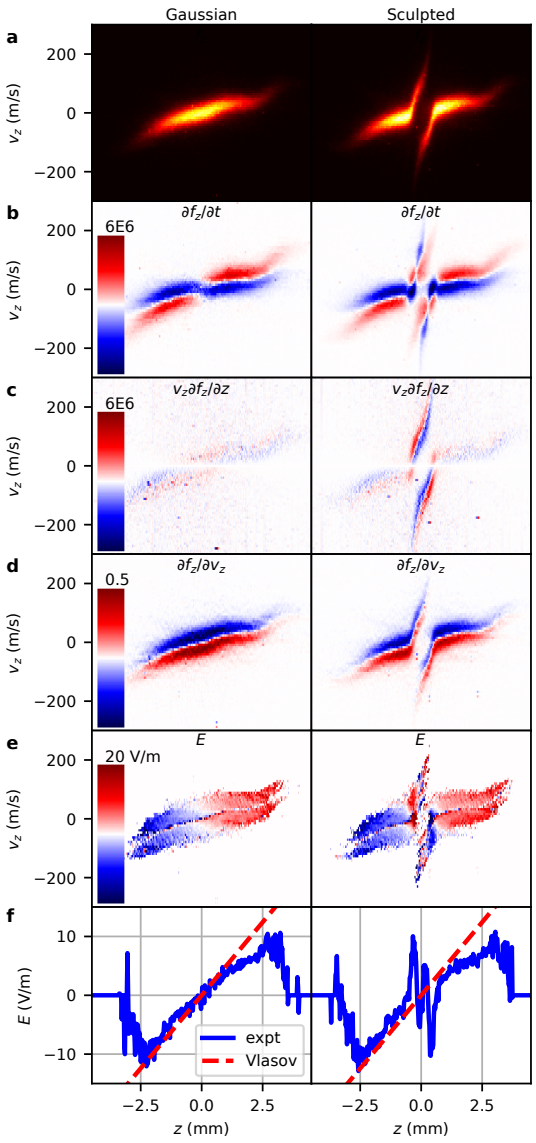

Figure 2.2 **a**) Gaussian (unsculpted) vs. sculpted plasma velocity distributions in phase space just after ionization. **b**) − **d**) Derivative terms of Boltzmann distribution (see Equation 2.3). **e**) Visual representation of the electric field in phase space. **f**) Relative magnitude of the electric field in the Vlasov approximation is plotted over the measured electric field from the experiment.

2.2 Relevance of UNP Data

Ultracold neutral plasmas were first created in the late 1990's by researchers at NIST, Dr. Bergeson being one of them [3]. Thus, UNPs are a relatively new field in plasma physics. While it is important to study UNPs for their own sake, there is also strong evidence that these plasmas can be used to understand certain dynamic aspects of high energy-density plasmas (HEDPs) like those created in the inertial confinement fusion (ICF) experiments performed at the National Ignition Facility (NIF) [11]. In fact, one of the motivations for improving BGK codes like the one described in Section 2.1 using data from UNPs is so that they may better simulate HEDPs. BGK models have been used to study HEDPs since at least the mid-1990's [12]. This connection between these seemingly disparate plasma regimes arises because UNPs and a subset of HEDPs exhibit similar degrees of strong coupling (where the Coulomb coupling parameter $\Gamma \geq 1$), meaning that the nearest-neighbor electrostatic potential is greater than the average thermal kinetic energy of the plasma. This gives rise to a liquid-like description, rather than a gas-like description of these plasmas.

Figure 2.3 shows the overlap of UNPs and HEDPs in the Coulomb coupling strength Γ and screening strength κ parameter-space. The Coulomb coupling parameter Γ measures the strength of electrostatic ion-ion interactions, while the screening strength κ characterizes the degree to which electrons shield those interactions, with larger κ indicating stronger electron screening and shorter-ranged effective interactions. These two dimensionless parameters determine the state of the plasma in the one-component Yukawa model [13], where the Yukawa pair potential is given as,

$$U(r) = \frac{Q_1 Q_2}{4\pi\varepsilon_0 a} \frac{e^{-\kappa(r/a)}}{r/a}, \quad \kappa \equiv \frac{a}{\lambda_D}. \tag{2.4}$$

where $a = \left(\frac{3}{4\pi n}\right)^{1/3}$ is the Wigner–Seitz radius and $\lambda_D = \sqrt{\frac{\varepsilon_0 k_B T_e}{n_e e^2}}$ is the Debye screening length for a single-species plasma. Although the Yukawa model does not account for all the expected

physics, especially quantum effects such as three-body recombination, bound states, and quantum degeneracy, UNPs and HEDPs share similar physics in these aspects as well [1].

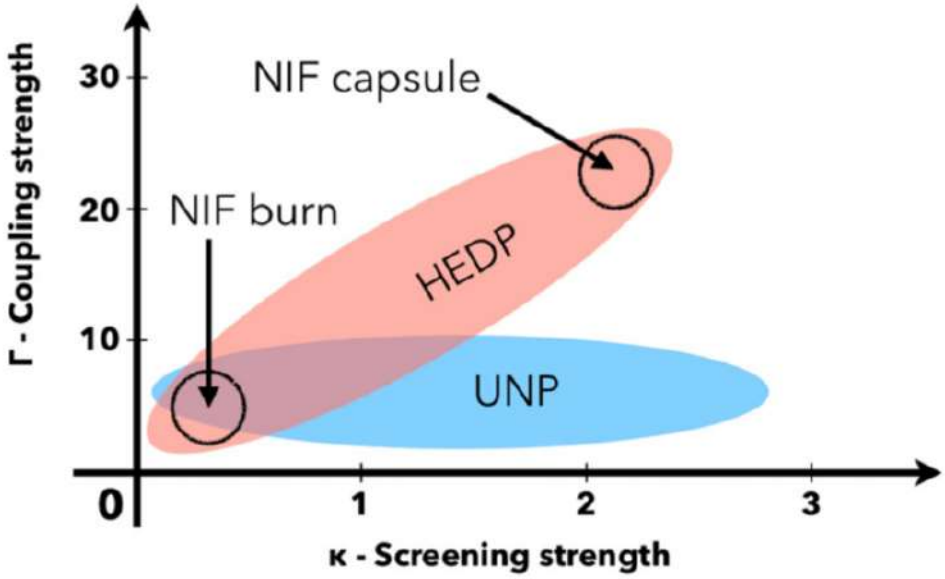

Figure 2.3 Diagram showing the shared regime of UNPs and HEDPs in Coulomb coupling strength Γ and screening strength κ parameter-space. Figure from [11].

Testing kinetic codes against UNP data is advantageous for many reasons. Firstly, UNPs are much more accessible than HEDPs in that they lend themselves to conventional, high-resolution diagnostics, such as direct imaging and laser spectroscopy. HEDP phenomena occur over timescales that are too fast to image directly, owing to the high temperatures and ion densities of these plasmas. Often, average ion-ion collision timescales are in the picosecond range [14]. UNPs, on the other hand, have a typical ion temperature of around 1 K and ion densities on the scale of $10^8 - 10^9\,\mathrm{cm}^{-3}$ (about $10-12$ orders of magnitude lower than HEDPs), giving them collision times on microsecond scales [11]. Moreover, the parameters that dictate the behavior of the plasma (electron temperature, charge state, density, etc.) are more tunable in UNPs. Finally, fundamental processes such as three-body recombination, electron–ion thermalization, collisional relaxation, and collective oscillations occur in both regimes. UNPs are thus a testbed where theories of transport coefficients, collision

operators, and kinetic-to-hydrodynamic transitions can be benchmarked before being applied to HEDPs.

2.3 Operating the Experiment

There are many components that must be precisely calibrated to create a UNP, in particular, laser wavelengths must be within a margin of error that is determined by the natural line width of the transition in question. For calcium, the 423 nm transition has a "generous" natural line width of 35 MHz, whereas the 397 nm and 866 nm transitions for ionized calcium have a natural line width of about 22 MHz. To reach this level of precision in our lab, a frequency comb is used.

The 2005 Nobel Prize was awarded to Ted Hänsch and John Hall for their contributions in the development of laser-based precision spectroscopy through the creation of the frequency comb. This invention bridged the gap between microwave/ radio frequencies (which are countable by electronics) and optical frequencies (which are not countable by electronics). A frequency comb is a laser that produces a train of ultrashort pulses in time, which translates into a spectrum of sharp, evenly spaced peaks in the frequency domain. These peaks (i.e., cavity modes) can then be used to ascertain the frequency of other lasers within its spectrum to within about 1 MHz. The n-th mode of the comb can be found using the relation,

$$f_n = f_{\text{offset}} + n f_{\text{rep}} \tag{2.5}$$

where f_{offset} is the carrier-envelope offset frequency and $f_{\text{rep}} = \frac{c}{L_{round\,trip}}$ is known as the free spectral range (FSR).To be able to give *definite* frequency information (as opposed to the distance in frequency-space relative to one of the drifting modes of the comb), there needs to be a reliable, well-defined anchor to serve as a reference point. This is found by locking a diode laser to a specific atomic transition in rubidium and then locking the nearest comb mode to the diode laser.

In our lab, mode locking is achieved through a mechanical "kick" generated by pulling and releasing a plunger that perturbs the laser cavity length. Whereas in a free-running laser cavity all of the longitudinal modes have phases that are random relative to one another, this kick perturbs the phases of all of the modes at the same time. If conditions are right, this sudden perturbation can seed constructive interference at one point in time, creating a spike in intensity (a pulse), which is then reconstructed with every round trip through the cavity. By overlapping this pulse train with the anchored diode laser, a beat note is formed with the comb's nearest cavity mode and, therefore, the frequency of every mode can be known.

The frequency comb in our lab has about $n = 30,000$ modes. Once the carrier offset is known, the frequency of any laser (within the comb's spectrum) can be discovered using a similar equation,

$$f_{\text{laser}} = f_{\text{offset}} + n f_{\text{rep}} \pm f_{\text{beat}} \tag{2.6}$$

The experiment carried out to gather data for the BGK project consists of neutral calcium atoms confined in a MOT, which is then ionized using two pulse lasers, much like the electron Penning trap. Before running the experiment, some preliminary measurements of laser power and environmental conditions are performed, as well as any necessary troubleshooting of the frequency comb, photodiodes, laser locks, dye lasers, etc. Once the lasers have been tuned against the reference of the frequency comb, the gate valve in front of the heated calcium sample is opened and the power source for the MOT coils is turned on. An atomic beam, slower laser, six trapping lasers, and quadrupole cusp trap are all that is required to form a MOT. Additional measurements of the MOT are taken by analyzing images of it as described in Section 3.2.1. After capturing the MOT data, the sample is ready to be ionized and probed.

The ionizing pulse lasers fire at 10 Hz and are triggered by a pulse generator, as are the fast-switch IGBT circuits and the ICCD camera. The 397 nm probe laser is scanned over a detuning range (generally $\pm$400 MHz from resonance) in 10 MHz intervals. At each frequency, a different

velocity class of ions will be Doppler shifted into resonance with the probe laser and give off a fluorescence signal, creating an image in the yz-plane. By combining the spatial signal information over all the velocity classes, and integrating the signal over a narrow band in the y direction (see Fig. 2.4), a phase-space plot of the plasma at a given delay time can be generated.

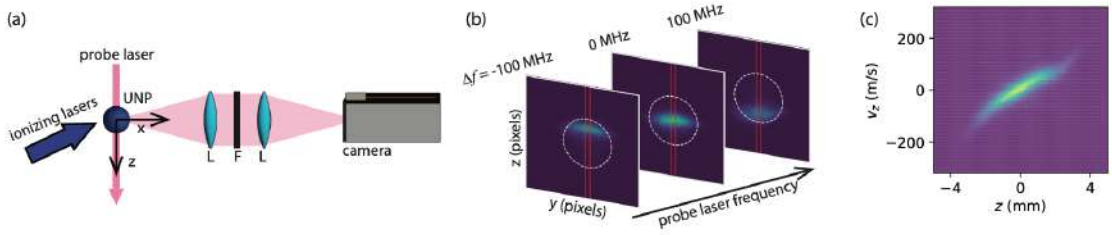

Figure 2.4 Experimental setup to generate phase-space fluorescence maps. (a) Fluorescence induced by the 397 nm probe laser is focused and imaged onto the ICCD camera sensor. (b) Images taken at different detunings of the probe laser to yield velocity class information. The dashed white circle indicates the size of the plasma. Dashed red lines mark the y-pixels that are averaged to give the one-dimensional slice in z. (c) Images at different detunings are superimposed to give the fluorescence map in z. Delay time is at $4\mu s$. This is a modified figure from [1].

Manually inputting the delay time in the pulse generator that triggers the ICCD camera allows for observation of the plasma at later times. The time evolution of the plasma in phase-space can then be visualized, as seen in Fig. 2.5. This is the data that our collaborators use to vet BGK codes. Other Boltzmann solvers (such as Fokker-Planck codes) have also been tested against our data, but to a lesser degree.

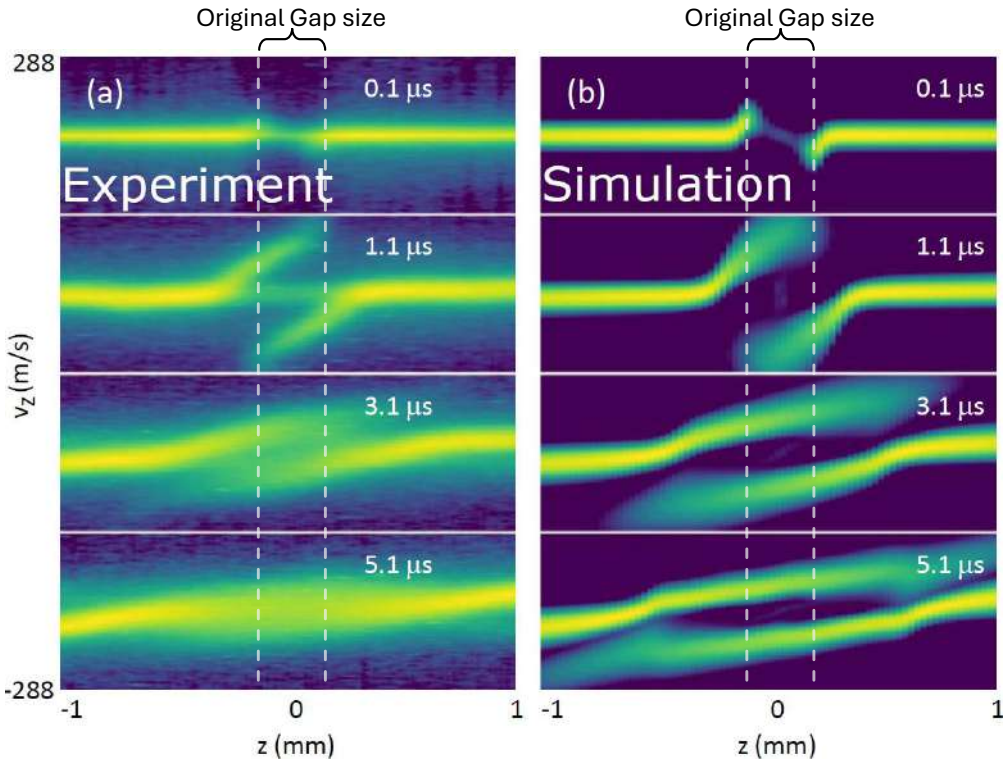

Figure 2.5 Comparison of experimental and simulated phase-space plots of a sculpted plasma. The dashed lines indicate the approximate size of the initial gap. Fluorescence intensity gives the relative number of ions in a location at a certain velocity class, with the strength of the fluorescence signal on a logarithmic scale. The ions at the edge of the gap experience the greatest acceleration due to the steep density gradient. As the plasma expands, the ions in the gap begin to thermalize and form a more Gaussian velocity distribution.

Chapter 3

Contributions to Group Projects and Acquired Skills

3.1 Group Projects

While most of my time in this program was spent working on the electron Penning trap and the BGK project, I did assist in other projects that were taken on by our laboratory. In particular, I aided in writing a comment on a paper involving molecular dynamics simulations of UNP expansion in a quadrupole magnetic field, and research into dielectric barrier discharge (DBD) plasmas for an experiment currently underway in our lab. Helping with these projects allowed me to broaden the scope of my research and learn about subjects outside of the main thrust of my thesis work.

3.1.1 Cusp Trap Paper

On the day of February 29, 2024, I, along with my fellow research assistants, sat down in Dr. Bergeson's office to write a comment on a paper published by Bronin et al. in 2023. In their paper, the authors presented results from molecular dynamics (MD) simulations of calcium

UNPs expanding in a quadrupole magnetic field. While the initial expansion behavior and electron confinement from their simulations agreed with experimental results taken in our lab some years prior, the simulations did not show certain dynamic oscillations in the plasma density. These oscillations can be seen in Fig. 3.1 and increase in amplitude at higher electron temperatures. Termed "breathing modes", these oscillations occur as a result of magnetic mirroring of the electrons.

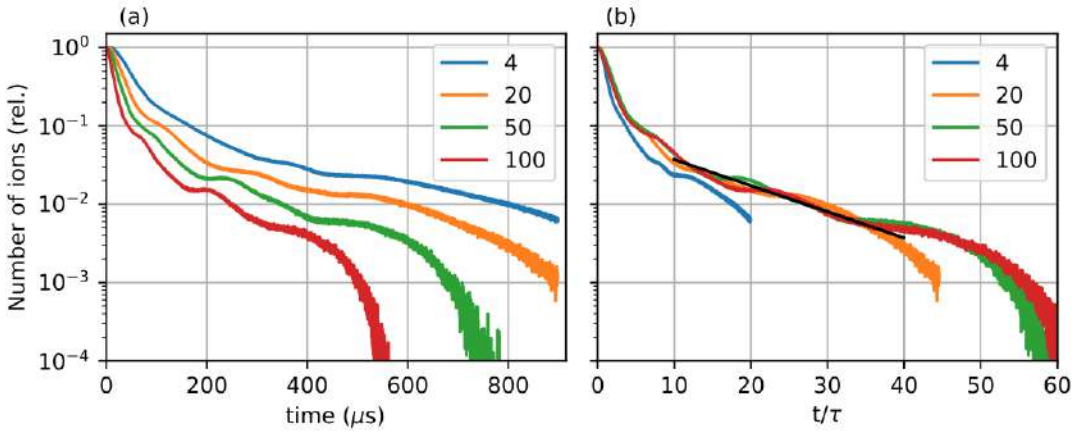

Figure 3.1 Example of longitudinal oscillations (or "breathing modes") of ion density in a UNP expanding in a quadrupole magnetic field. a) Relative number of ions as a function of time at different electron temperatures. b) Relative number of ions as a function of scaled time of the plasma. This figure is from [10].

The authors of the paper suggested that the trap lifetime could be increased by augmenting the cusp trap with lasers to cool the ions and reduce the rate at which they leak out of the trap. However, because the trap becomes more non-neutral over time, it is improbable that adding weak optical forces will have any appreciable effect. Moreover, it was found from our data that ionization using a continuous-wave laser did not increase the lifetime of the trap as shown in the simulations [10]. Our results were in accordance, however, in that increasing the strength of the magnetic field did not increase the trap lifetime. The cusp trap lifetime scales as $T_e^{-1/2}$.

3.1.2 Plasma Bullet

During the summer of 2024, Dr. Bergeson had our research group begin preparatory research into dielectric barrier discharge (DBD) plasmas and various adaptations of Boltzmann solvers in response to a project that had been proposed (and was later funded) by the U.S. army. This venture came to be known as the "plasma bullet" project, and explores the electron density of DBD plasmas using precision spectroscopy. Figure 3.2 shows the setup of this experiment and the bullet-like discharge that is generated.

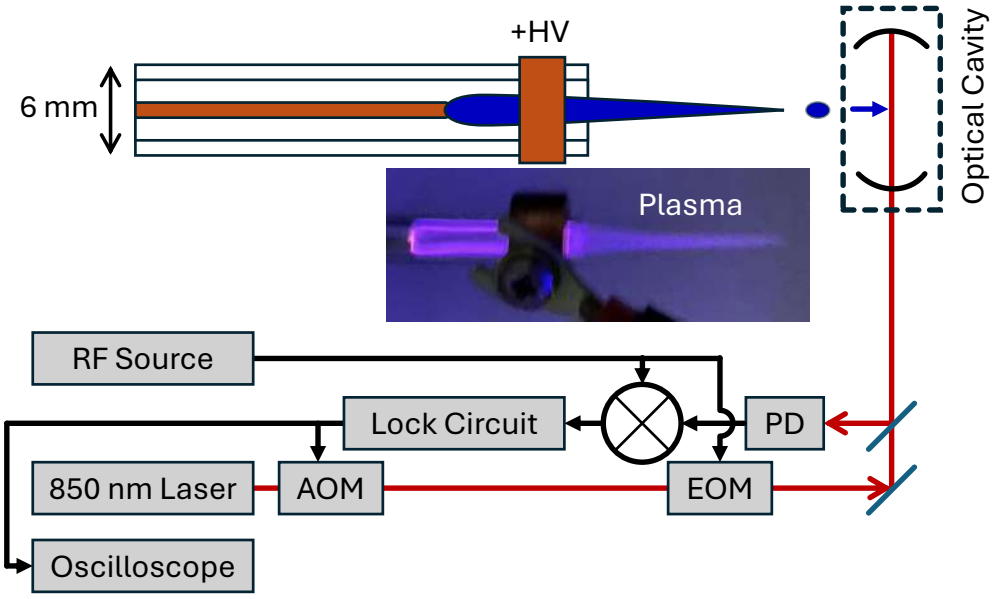

Figure 3.2 DBD plasma bullet experiment in our laboratory. The dielectric is a quartz glass tube that surrounds the grounded electrode. The phase shift of the laser in the optical cavity provides information on the refractive index of the plasma, which is proportional to the electron density.

A DBD plasma is a type of non-thermal, atmospheric-pressure plasma generated between two electrodes separated by at least one insulating dielectric layer. When an alternating high voltage is applied, micro-discharges form across the small gas gap, producing a diffuse plasma without developing into a continuous arc. The dielectric barrier limits the current, quenches individual

micro-discharges, and allows the plasma to be sustained over many voltage cycles without damaging the electrodes.

The aim of the plasma bullet experiment is to determine the electron density of the plasma by measuring the phase shift of a probe laser that passes through it. When a laser propagates through a plasma, its phase is shifted due to the plasma's refractive index. The refractive index of a collisionless plasma is,

$$n = \sqrt{1 - \frac{\omega_p^2}{\omega^2}} \tag{3.1}$$

where ω is the laser frequency and,

$$\omega_p = \sqrt{\frac{n_e e^2}{\varepsilon_0 m_e}} \tag{3.2}$$

is the plasma frequency. The electron density is n_e. The phase accumulated by the laser after traversing a plasma of thickness L is,

$$\phi = \frac{2\pi}{\lambda} nL, \tag{3.3}$$

so the resulting phase shift is therefore,

$$\Delta\phi = \phi - \phi_0 = \frac{2\pi}{\lambda}(n-1)L. \tag{3.4}$$

With this relationship we can solve for the electron density,

$$n_e \approx -\frac{\Delta\phi\, \varepsilon_0 m_e\, \omega^2\, \lambda}{\pi e^2 L}. \tag{3.5}$$

Over the course of this summer, I took part in weekly meetings where we discussed DBD plasmas and gave presentations on findings from our research. In total, I ended up giving six

presentations on DBD plasmas and methods of modeling kinetic plasmas. The presentations were based on the following papers:

- Zhou, Di, et al. "Application of a gas-kinetic BGK scheme in thermal protection system Analysis for hypersonic vehicles." Entropy 24.10 (2022): 1325.
- Agrawal, Samarth, S. K. Singh, and Santosh Ansumali. "Fokker–Planck model for binary mixtures." Journal of Fluid Mechanics 899 (2020): A25.
- Evans, Ben. "Nano-particle drag prediction at low Reynolds number using a direct Boltzmann–BGK solution approach." Journal of Computational Physics 352 (2018): 123-141.
- Opaits, D. F., et al. "Surface charge in dielectric barrier discharge plasma actuators." Physics of Plasmas 15.7 (2008).
- Mitchell, N. T., et al. "A reduced kinetic method for investigating non-local ion heat transport in ideal multi-species plasmas." Plasma Physics and Controlled Fusion 66.7 (2024): 075005.
- Viegas, Pedro, et al. "Interaction of an atmospheric pressure plasma jet with grounded and floating metallic targets: simulations and experiments." Plasma Sources Science and Technology 29.9 (2020): 095011.

3.2 Skills Developed Throughout the Program

During my time in this program, taking graduate-level courses and working in Dr. Bergeson's laboratory gave me the opportunity to gain experience in many areas that I did not have a chance to develop when I was pursuing my Bachelor's degree at BYU–Idaho. I had the fortune to practice the theory of physics as well as the hands-on practical application of it. These skills not only taught me how to solve physics problems, but how to be better at solving problems in general.

3.2.1 Programming

When I began working in the lab, I quickly realized that I did not have adequate experience with programming to effectively process data. To help with this, my first project was to take a MATLAB code used for analyzing the MOT and convert it into a python script. This would allow all data analysis in the lab to be done using Python. The program took data from 20 .bmp files of the MOT (see Fig. 3.3), averaging five images of the following four possible assignments:

- No MOT, probe laser off
- MOT on, probe laser off
- No MOT, probe laser on
- MOT on, probe laser on

The program also had an interactive portion where the user had to manually select points on an image via graphical input functions, as shown in Fig. 3.4. The information from these interactions was then used to finish calculations for the MOT. This project was the first time I had used the Python programming language.

Throughout my coursework, I have been challenged to solve a myriad of physics problems using different programming languages. In particular, I have grown accustomed to using Python, Mathematica, and MATLAB. I also gained some exposure to LabView (as many of the systems in the lab are programmed in this language) and Lua when, as previously mentioned, a script was written for the SimIon® software. Due to complex numerical problems being integrated into the curriculum for many of the courses in the graduate physics program, as well as courses (like Computational Physics) that are dedicated to learning this skillset, computational programming is a tool I now use confidently to solve problems.

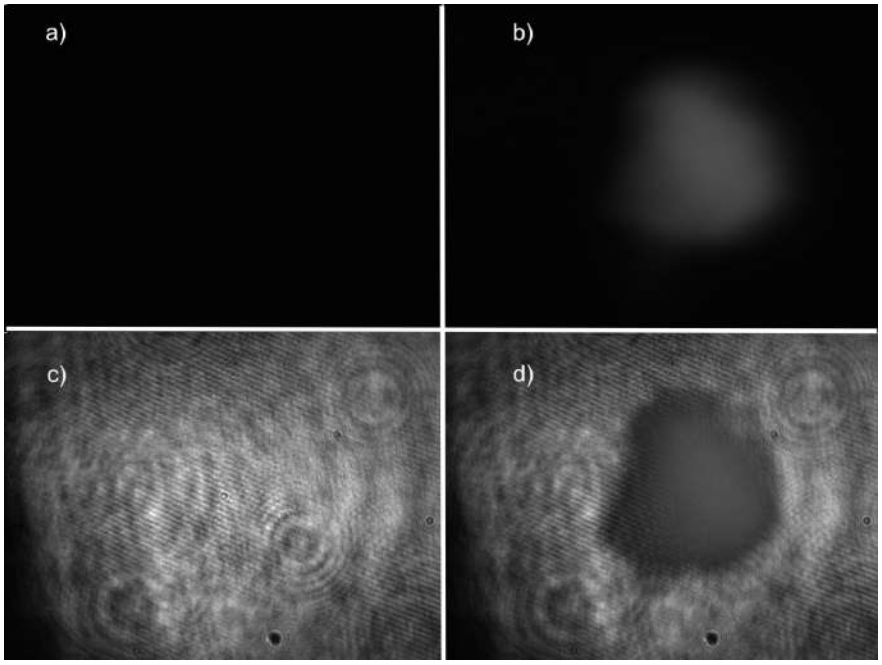

Figure 3.3 Images used to determine size, peak density, and optical properties of the MOT. a) No MOT, probe laser off (background noise), b) MOT on, probe laser off, c) No MOT, probe laser on, d) MOT on, probe laser on.

3.2.2 Vacuum Chamber Design and Construction

As described in Section 1.2, the first step in building the electron Penning trap was the construction of the vacuum chamber. Through the process of building and maintaining this vacuum chamber, I gained practical experience in how such systems are constructed, sealed, and evacuated, as well as the materials that can and cannot be used to do so. Beyond learning the basics of building HV and UHV systems (gaskets, torque specifications for conflat flanges, coordinating valve/ pump procedures, etc.), I also helped design and assemble custom pieces, such as the nozzle for the atomic beam (see Fig. 3.5) and the fragile electrical feedthroughs. The layout of the chamber itself also presented its own challenges, since heaters, pumps, valves, cables, chilled-water tubing, and support structures all had to fit together while leaving room for the considerable amount of optics components needed for the experiment.

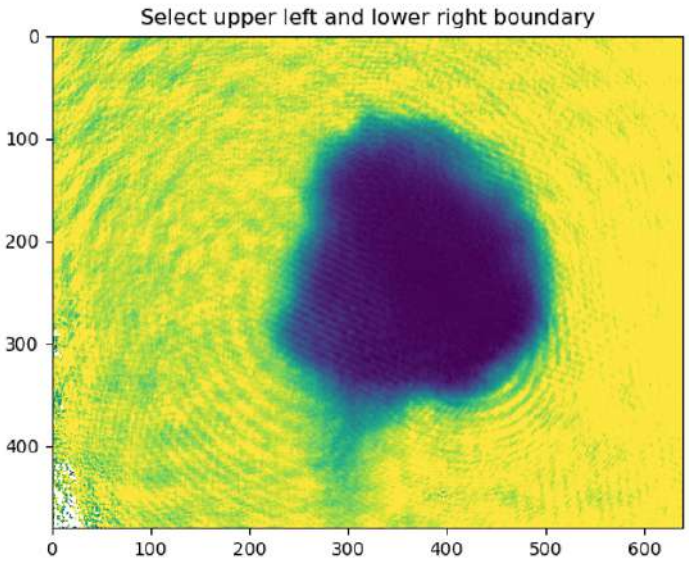

Figure 3.4 Interactive portion of the MOT analysis program.

The electrical components of the chamber were particularly problematic, as the chamber itself had to remain insulated from any wires or electrodes inside. Planning for these details and having a more robust design for internal electrical connections would have saved the chamber from having to opened many times for repairs. This hands-on experience gave me a much deeper appreciation for the engineering that underlies sensitive physical experiments, beyond what could be learned from theory alone.

3.2.3 Building Electrical Circuits

As someone who had only seen diagrams of electrical circuits in textbooks on electricity and magnetism, learning how to actually build a functional and safe circuit was invaluable. The circuits that Tucker Sprenkle built to run the MOT coils and uniform magnetic field coils in the chamber served as templates for the circuits that I built for the electron Penning trap. Some alterations to

Figure 3.5 Close-up of the custom-made nozzle flange. The 120 small tubes in the nozzle had to be placed by hand.

these circuits were made, though, requiring an understanding of the principles governing the physics, rather than a simple ability to replicate a schematic.

The resistive components used in these circuits had to be water cooled due to the high current required for the experiment. To do this, I worked with the machine shop to create custom aluminum pieces that the electrical components could be fastened onto. Connecting the chilled water lines in the lab to the circuits presented many problems over my last year in the program, but through it, I was able to gain useful experience in plumbing along with hard-learned lessons about hydrodynamics.

Building specialized electrical circuits not only taught me how to apply the principles of electricity and magnetism in a hands-on setting, but it also gave me valuable experience working with industry-standard equipment such as power supplies, high current resistors, varistors, rectifiers (diodes), and oscilloscopes, among others. Through this process, I became familiar with the kinds of tools and techniques that practicing physicists and engineers rely on. It also gave me insight into

Figure 3.6 Circuit that controls the MOT coils.

the companies and technologies that supply this equipment, broadening my perspective on how academic research connects with the larger scientific and industrial community.

3.2.4 Optics Design

UNPs require delicate calibration of all the optical components involved, including (but not limited to) mirrors, lenses, acousto-optic modulators, photodiodes, frequency doubling cavities, the frequency comb, gain crystals, Brewster angle windows, wave plates (quarter and half), polarizing beamsplitter cubes (or pol-cubes), apertures, dichroic filters, and bandpass filters. Building the electron Penning trap and collecting data for the BGK project gave me ample experience with all of these. I have learned to build optics designs using telescopes (discussed in more detail in Section 1.6.2), retroreflective mirrors (discussed in Section 1.3), periscopes, and dichroic filters, as well as using half-wave plates and pol-cubes to generate multiple beams of equal frequency.

Figure 3.7 Custom copper solenoid used as the "dummy coil" in the ramp-up stage of the bias coil circuit. The solenoid carries both water and electrical current.

Mode matching beams into fiber optic cables, frequency doubling cavities, and photodiodes (to produce beat notes) is also essential. The success of these experiments hinges on being able to control the size, shape, polarization, and frequency of the lasers. It is also imperative to be able to troubleshoot issues when dealing with sensitive optical equipment.

In addition to aligning and shaping laser beams, I also learned to focus images onto cameras and photocathodes while filtering out the scattered light with telescopes and apertures. Because all the ports in the chamber were being used as windows for different lasers, off-axis mirrors had to be used to image the MOT onto a Blackfly camera. Precise measurements were made to focus the image through a lens such that the image of the MOT corresponded to its actual size.

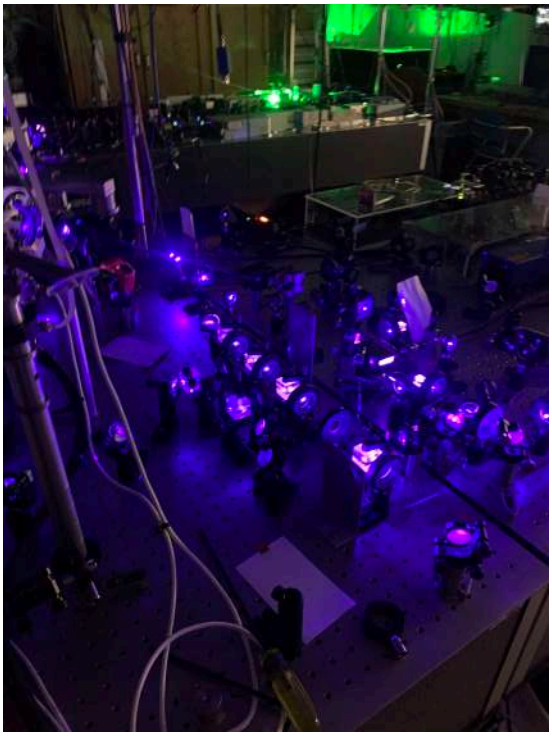

Figure 3.8 Photo of scattered light from the 423 nm laser used to trap atoms in the MOT. A series of half-wave plates and pol-cubes was used to split this laser into the three orthogonal trapping lasers.

3.2.5 Laser Cavity Design

In the Lasers and Atoms class I took from Dr. Bergeson, I learned about the theory of optical cavity design and then how to actually construct one. I aided in making a laser cavity using a Ti:Sapphire crystal. The cavity itself utilized two concave mirrors and two flat mirrors in a "bowtie" configuration, shown in Fig. 3.9.

Before the laser enters the cavity, a lens of focal length f is placed a distance d away from the input coupling mirror. Using the ABCD formalism for the intracavity eigenmode, we were able to correct for astigmatism by finding the proper angle of incidence and distance to place the curved mirrors from the gain medium that would cause the Rayleigh range of the sagittal and tangential planes to be equal. Then using the system of equations,

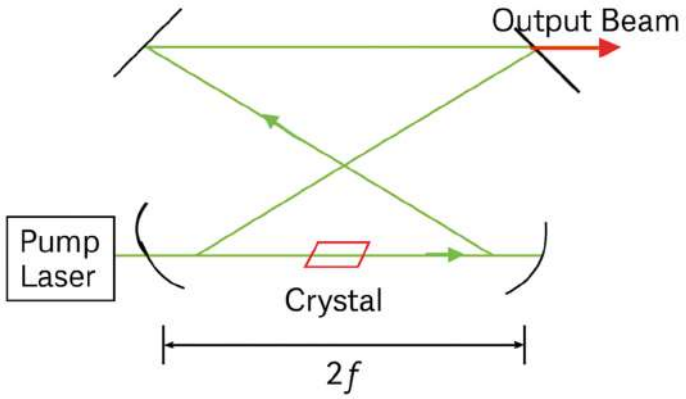

Figure 3.9 Diagram of a "bowtie" laser cavity.

$$ACz_0^2 + BD = 0, \qquad z_0' = \frac{z_0}{C^2 z_0^2 + D^2} \tag{3.6}$$

we were able to find values of $f = 362\,\text{mm}$ and $d = 310\,\text{mm}$ to maximize the input coupling efficiency (i.e., mode matching). By applying these parameters, we were able to achieve the output power seen in Fig. 3.10.

3.2.6 Presenting Scientific Research

Over the course of my program, I had the opportunity to present scientific research in a number of different settings. I gave several short presentations to our research group as described in Section 3.1.2. I also gave a presentation of my prospectus to my thesis committee, two presentations at BYU student research conferences (2024 & 2025), and a formal presentation at the annual APS Division of Plasma Physics (DPP) conference in Atlanta, GA. As someone who is not naturally comfortable speaking in public (much less fielding questions from experts in the area I am reporting on), these opportunities pushed me to challenge myself and grow as a scientist.

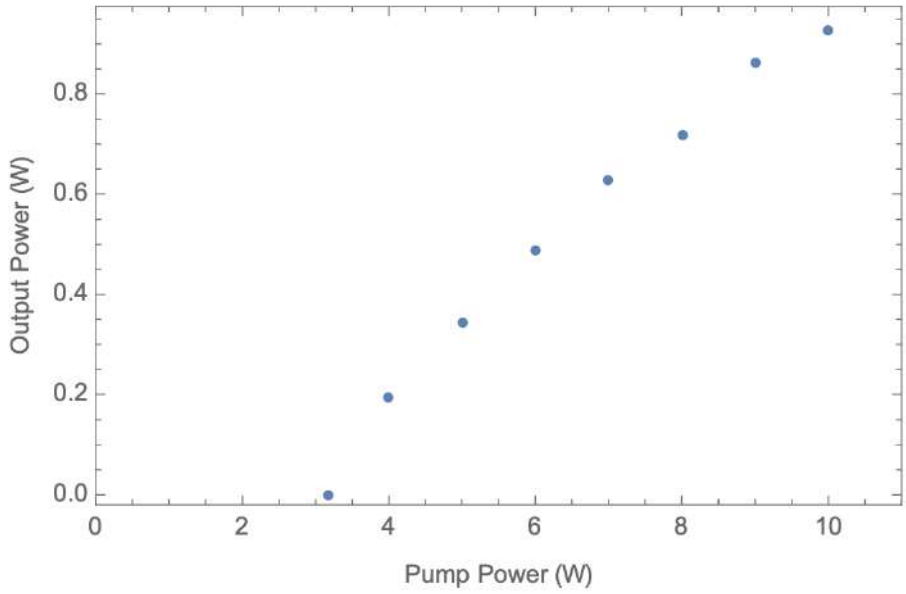

Figure 3.10 Plot of the pump power vs. output power of the Ti:Sapphire laser cavity made during a group project in my Lasers and Atoms course.

3.2.7 Papers Published

During my time at BYU, I had the opportunity to coauthor three papers. They are:

- "Non-equilibrium phase-space dynamics of a strongly-coupled plasma with steep density gradients," B. Farley, M. Schlitters, D. Sieverts, M. Miller, S. Bergeson, M. Murillo, and J. Haack, 66th Annual Meeting of the APS Division of Plasma Physics, Atlanta, GA, October 2024 [15]

  This was the abstract for my presentation at the APS DPP conference talk in 2024. The abstracts for all the presentations are posted on the "Bulletin of the American Physical Society" on the APS website. This presentation explained findings from the BGK project.

- "Comment on 'Ultracold plasma expansion in quadrupole magnetic field'," M. Schlitters, M. Miller, B. Farley, and S. D. Bergeson, Phys. Rev. E 110, 027201 (2024) [10]

This paper was a response to an article by Bronin et al. reporting findings from computer simulations of UNPs in quadrupole magnetic fields, as explained in Section 3.1.1.

- "Experimental and computational study of phase space dynamics in strongly coupled plasmas with steep density gradients," Phys. Plasmas 32, 032104 (2025) [1]

  This paper reported our findings from the BGK project, as described in Chapter 2.

3.2.8 Supervising Undergraduate Students

The skill that I most enjoyed developing was that of teaching and orienting new students in the laboratory. I was privileged to work with several talented and genial undergraduate students who helped me immensely in a number of ways. Building the electron Penning trap and all of the ancillary equipment, as well as setting up the necessary software required a lot of work. Looking to Dr. Bergeson as my example, I quickly learned how to delegate tasks to my fellow research assistants and supervise the execution of those tasks. Together, we worked to implement an agile project management approach, which included a Kanban board and regular "scrum" meetings, or stand-ups. I also learned that no matter how busy I was, I could always take time to answer pertinent questions regarding scientific or practical matters. I wanted to make those I supervised feel heard and recognized the way I did by my mentor and professors.

In addition to the direct support I received from the undergraduate students in the laboratory, they also helped me indirectly by asking good questions about our work. Explaining the experimental methods and physical phenomena at play in the plasma experiments helped me to identify gaps in my own knowledge and then solidify my understanding of them. I also learned that being a good leader includes learning from those you supervise and being open to ideas. This openness was present at all levels in our laboratory. The dynamic amongst myself, my coworkers, and my superiors taught me how a professional scientific workplace should function.

Appendix A

Retroreflecting Through a Quarter-Wave Plate

Let the Jones vectors for right- and left-circular polarization be

$$\mathbf{e}_R = \frac{1}{\sqrt{2}} \begin{bmatrix} 1 \\ -i \end{bmatrix}, \qquad \mathbf{e}_L = \frac{1}{\sqrt{2}} \begin{bmatrix} 1 \\ i \end{bmatrix}.$$

A quarter-wave plate (QWP) with its fast axis along x is represented by

$$Q(0) = \begin{bmatrix} 1 & 0 \\ 0 & i \end{bmatrix}.$$

A mirror at normal incidence contributes only a global phase factor, so we can write its Jones matrix as

$$M = e^{i\phi} I,$$

where I is the identity matrix and ϕ is an irrelevant phase.

The round-trip through the same QWP is then

$$\mathbf{E}_{\text{out}} \propto Q(0)\, M\, Q(0)\, \mathbf{e}_R = Q(0)^2\, \mathbf{e}_R = \begin{bmatrix} 1 & 0 \\ 0 & -1 \end{bmatrix} \frac{1}{\sqrt{2}} \begin{bmatrix} 1 \\ -i \end{bmatrix}.$$

Carrying out the multiplication, we find

$$\mathbf{E}_{\text{out}} = \frac{1}{\sqrt{2}} \begin{bmatrix} 1 \\ i \end{bmatrix} = \mathbf{e}_L.$$

Thus,

$$Q(0)\,M\,Q(0) = Q(0)^2$$

acts as a half-wave plate, which flips the handedness:

$$\mathbf{e}_R \longleftrightarrow \mathbf{e}_L.$$

For an arbitrarily oriented QWP,

$$Q(\theta) = R(-\theta) \begin{bmatrix} 1 & 0 \\ 0 & i \end{bmatrix} R(\theta),$$

we similarly have

$$Q(\theta)^2 = H(\theta),$$

where $H(\theta)$ is the Jones matrix of a half-wave plate, and

$$H(\theta)\,\mathbf{e}_R = \mathbf{e}_L, \quad H(\theta)\,\mathbf{e}_L = \mathbf{e}_R.$$

Bibliography

[1] S. Bergeson, M. Schlitters, M. Miller, B. Farley, D. Sieverts, M. S. Murillo, and J. R. Haack, "Experimental and computational study of phase space dynamics in strongly coupled plasmas with steep density gradients," Phys. Plasmas **32,** 032104 (2025).

[2] Savard *et al.*, "A new cooling technique for heavy ions in a Penning trap," Physics Letters A **158,** 247–252 (1991).

[3] T. Killian, S. Kulin, S. Bergeson, L. Orozco, C. Orzel, and S. Rolston, "Creation of an Ultracold Neutral Plasma," Phys. Rev. Lett. 83 (1999).

[4] R. Sprenkle, S. Bergeson, L. Silvestri, and M. Murillo, "Ultracold neutral plasma expansion in a strong uniform magnetic field," Phys. Rev. E 105 (2022).

[5] Erickson, Alexander, and S. Bergeson, "Dual Species Calcium and Ytterbium Magneto Optical Trap," Journal of Undergraduate Research **2016,** 229 (2016).

[6] P. Ungar, Jeffery, D. Weiss, E. Riis, and S. Chu, "Optical molasses and multilevel atoms: theory," Journal of the Optical Society of America B **6,** 2058–2071 (1989).

[7] R. T. Sprenkle, "Temperature relaxation and magnetically suppressed expansion in strongly coupled ultracold neutral plasmas," Ph.D. dissertation (2021).

[8] C. Pak, V. Billings, M. Schlitters, S. Bergeson, and M. S. Murillo, "Preliminary study of plasma modes and electron-ion collisions in partially magnetized strongly coupled plasmas," Phys. Rev. E 109 (2024).

[9] G. M. Gorman, M. K. Warrens, S. J. Bradshaw, and T. C. Killian, "Magnetic Confinement of an Ultracold Neutral Plasma," Phys. Rev. Lett. **126,** 085002 (2021).

[10] M. Schlitters, M. Miller, B. Farley, and S. Bergeson, "Comment on "Ultracold Plasma Expansion in Quadrupole Magnetic Field"," Phys. Rev. E. **110,** 027201 (2024).

[11] S. Bergeson, S.Baalrud, C. Ellison, E. Grant, F. Graziani, T. Killian, M. Murillo, J. Roberts, and L. Stanton, "Exploring the crossover between high energy-density plasma and ultracold neutral plasma physics," Phys. Plasmas **26,** 100501 (2019).

[12] V. D. Levchenko, Y. S. Sigov, and F. Premuda, *Numerical study of non-ideal Vlasov-BGK plasmas* (Stevens Institute of Technology, Hoboken, NJ (United States), 1995).

[13] R. T. Farouki and S. Hamaguchi, "Thermodynamics of strongly-coupled Yukawa systems near the one-component-plasma limit. II. Molecular dynamics simulations," J. Chem. Phys. 101 (1994).

[14] A. Richardson, *NRL Plasma Formulary* (U.S. Naval Research Laboratory, Washington, DC, 2019).

[15] 66th Annual Meeting of the APS Division of Plasma Physics, Atlanta, GA, October 2024 .